This paper describes objective technical results and analysis. Any subjective views or opinions that might be expressed in the paper do not necessarily represent the views of the U.S. Department of Energy or the United States Government.

SAND2015-0988J

Continuous joint measurement and entanglement of qubits in remote cavities

Felix Motzoi,[1,2,3] Mohan Sarovar,[4] and K. Birgitta Whaley[1,2]

[1] *Berkeley Center for Quantum Information and Computation, Berkeley, California 94720 USA*
[2] *Department of Chemistry, University of California, Berkeley, California 94720 USA*
[3] *Department of Physics, University of California, Berkeley, California 94720 USA*
[4] *Department of Scalable and Secure Systems Research, Sandia National Laboratories, Livermore, CA 94550 USA*

(Dated: January 29, 2015)

Two superconducting qubits in spatially separated microwave cavities were entangled recently by a sequential probe of the two cavities by a coherent mode [Roch *et al.*, Phys. Rev. Lett. 112, 170501 (2014)]. In this paper we derive the theory describing this experiment from first principles, and fully characterize the weak measurement induced dynamics and entanglement generation. This allows us to identify the limitations of the current experiment and suggest improvements that enable the generation of higher degree of entanglement between the qubits.

I. INTRODUCTION

Entanglement between remote parties is a key resource in many quantum information applications, including quantum teleportation, quantum key distribution, and quantum metrology, and is central to the notion of a *quantum network* [1]. Distributed entangled states are also a critical component for scalable quantum computing since they enable long-range gates between spatially separated qubits [2]. Accordingly many different approaches have been proposed to distribute or generate entangled states among systems that are significantly spatially separated. Distributing entangled states after preparation at a central location is practically challenging since decoherence in distribution channels typically degrades entanglement, *e.g.*, [3, 4]. Alternatively, a long-range coupling between remote systems can be engineered by exchanging single quanta, and entanglement can be generated this way, as has been recently demonstrated for atoms, photons and combinations thereof [5, 6].

A fundamentally distinct approach for preparing entangled states of systems residing at remote locations is to perform a *joint measurement* on them. Most proposals for achieving such joint-measurement-enabled entanglement interfere photons that are spontaneously emitted by atoms (or artificial atoms) in such a way that subsequent detection of a photon makes the identity of the emitter indiscernible, *e.g.*, [7–12], and thus projects the remote atoms into an entangled state. The degree of entanglement generated is heavily dependent on the quality and stability of the interferometer and efficiency of detection of spontaneously emitted photons. As a result achieving high fidelity entangled states with this approach is challenging, although several proof-of-principle experiments have demonstrated validity of the approach [13, 14]. An alternate approach is to perform a joint measurement by sequentially interacting two systems with a coherent light mode. This has been explored as method for generating entanglement theoretically [15, 16] and experimentally implemented using collective excitations of atomic clouds [17]. Most recently, a sequential probe has been utilized to probabilistically entangle superconducting qubits in separate microwave cavities [18], and in this work we develop a theoretical description of that experiment from first-principles and analyze in detail the potential and limitations of entanglement generation in this apparatus.

In the dispersive interaction regime, a coherent mode reflected off a cavity with an embedded qubit acquires a phase shift that depends on the internal state of the qubit. This motivates the essential idea behind the entanglement generation scheme we study here, namely, to perform a measurement of the parity of the qubit pair excitation state by sequentially probing the two cavities that contain them. This is achieved by performing a homodyne measurement of the total phase acquired by the twice-reflected probe field, as described in detail in Ref. [18]. Fig. 1 shows a schematic of the apparatus. Ideally, the qubit observable that corresponds to this measurement, which we shall refer to as a half-parity measurement, takes the form $O_{hp} = \sigma_z^1 + \sigma_z^2$, where σ_z^i is the Pauli-Z operator on the ith qubit. This observable cannot distinguish between the qubit basis states $|01\rangle$ and $|10\rangle$ [1]. Therefore if the initial state of the two qubits is the equal superposition state $|\Psi_0\rangle = \frac{1}{2}(|00\rangle + |01\rangle + |10\rangle + |11\rangle)$, the ideal half-parity measurement will yield the states $|00\rangle$ or $|11\rangle$, each with a probability 1/4, or the state $\frac{1}{\sqrt{2}}(|01\rangle + |10\rangle)$ with probability 1/2. This is to be distinguished from the full parity measurement of $O_{fp} = \sigma_z^1\sigma_z^2$, which yields the states $\frac{1}{\sqrt{2}}(|00\rangle + |00\rangle)$ and $\frac{1}{\sqrt{2}}(|01\rangle + |10\rangle)$ with equal probabilities. In the following we develop a detailed model of this sequential probe measurement from first principles, including all non-idealities present in the experiment of Ref. [18]. Although we develop the model within the context of the superconducting qubit experiment of Ref. [18], it applies more generally to any implementation of cavity-QED, including in the optical domain.

[1] Here, and in the following, for conciseness we omit tensor products when writing multiparty states.

Sandia National Laboratories is a multimission laboratory managed and operated by National Technology & Engineering Solutions of Sandia, LLC, a wholly owned subsidiary of Honeywell International Inc., for the U.S. Department of Energy's National Nuclear Security Administration under contract DE-NA0003525.

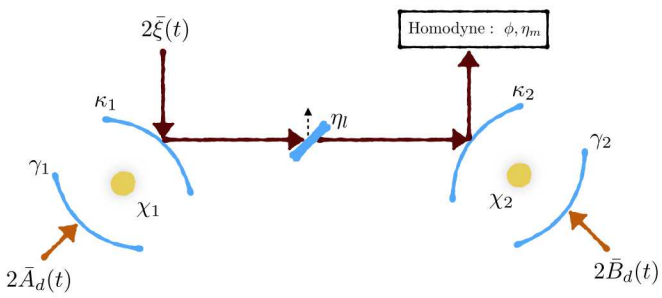

FIG. 1: Sequenctial probe of two spatially separated cavities with qubits (coupled dispersively to the fundamental cavity mode with strength χ_i). The cavities are asymmetric with the *kappa* ports being more transmissive than the γ ports. The beam-splitter between the cavities models the losses induced by the circulator that enforces one-way field propagation between cavities. We allow for arbitrary coherent state drives ($2\bar{A}_d(t)$ and $2\bar{B}_d(t)$) into the weakly coupled ports of both cavities. The field reflected off both cavities is measured by a homodyne detector with efficiency $\eta_{\rm m}$ and at a phase ϕ with respect to the probe $2\bar{\xi}(t)$.

The remainder of the paper is structured as follows. Section II A presents the dynamical model for full system derived from cascaded systems theory [19–21]. Then in section II B we perform a two-cavity polaron transformation on the model to obtain an exact, dressed description for the qubits alone that is easier to simulate than the full dynamical model. This polaron transform and subsequent derivation of an effective master equation for the dressed qubits constitutes a generalization of the methods first presented in Ref. [22]. In Sections II C and II D we demonstrate the qubit-reduced dynamics in the laboratory frame, including the loss and revival of entanglement between qubits. Section III further derives physical requirements and criteria for generating entanglement between the remote qubits. Section IV provides simulation data for a range of realistic experimental parameters and discusses the viability of obtaining high-grade concurrence betwen the qubits. Section V analyzes the effect population shifts during the continuous measurement and how to circumvent them. Section VI provides a summary and assessment of the benefits and possible extensions of this approach to other quantum processing tasks for superconducting qubits.

II. DERIVATION OF THEORETICAL MODEL

A. Full model of cascaded cavities

Consider the apparatus shown in Fig. 1. Each cavity has two ports, with asymmetric transmittivities. The "input" port on each cavity is low transmitivity (γ_i) and the "output" port is high transmittivity (κ_i). The probe field $\bar{\xi}(t)$ interfaces with the output ports of both cavities a distance L apart (in [18] a distance $L = 1.3$m was achieved), before impinging on the homodyne detector. The cavities are operated in the dispersive regime, where the Hamiltonians in the two cavities are given by

$$\begin{aligned} H_A &= \Delta_1 \mathbf{a}^\dagger \mathbf{a} + \chi_1 \mathbf{a}^\dagger \mathbf{a} \boldsymbol{\sigma}_z^1, \\ H_B &= \Delta_2 \mathbf{b}^\dagger \mathbf{b} + \chi_2 \mathbf{b}^\dagger \mathbf{b} \boldsymbol{\sigma}_z^2, \end{aligned} \tag{1}$$

respectively, where $\mathbf{a}(\mathbf{b})$ is the annihilation operator for the mode in cavity 1(2), $\boldsymbol{\sigma}_z^{1(2)}$ is the Pauli z operator for qubit 1(2), $\Delta_i \equiv \omega_d - \omega_r^i$ is the detuning of cavity i from the probe field $\bar{\xi}(t)$, and χ_i is the qubit-cavity coupling in the dispersive regime. These Hamiltonians are in the interaction frame with respect to the free Hamiltonians for the qubits: $-\frac{\omega_1}{2}\boldsymbol{\sigma}_z^1 - \frac{\omega_2}{2}\boldsymbol{\sigma}_z^2$. The input ports for the two cavities can also be used for driving the cavity or qubits at their respective frequencies (with fields $\bar{A}_d(t)$ and $\bar{B}_d(t)$, respectively), for state initialization and tomography. We will see that the coherent drive $\bar{B}_d(t)$ will be useful for compensating against asymmetries in the parameters between the two cavities and qubits. To minimize back-reflection of the probe field and ensure its unidirectionality, a circulator is inserted between the two cavities. Losses associated to this circulator will be included in the model developed below. The parameters of the system, including cavity transmitivities, losses, cavity coupling, are labeled in Fig. 1.

The dynamical model for the apparatus described in Fig. 1 can be derived using the cascaded cavity theory of Gardiner and Carmichael [19, 20], or by the modern SLH quantum network theory [21, 23]. We utilize the latter here and Fig. 2 presents an SLH network diagram that is equivalent to the apparatus in Fig. 1. G_1, G_2 and G_3 represent coherent displacements of the input vacua, G_4 and G_6 represent the cavity-qubit systems, and G_5 represents a beamsplitter modeling the lossy circulator. The output field $z(t)$ emerges from the output port of cavity 2 and is monitored by homodyne detection (see below). The SLH triples (S, L, H) [21, 23, 24] for these blocks are

$$\begin{aligned} G_1 &= \left(1, 2\bar{\xi}(t), 0\right) \\ G_2 &= \left(1, 2\bar{A}_d(t), 0\right) \\ G_3 &= \left(1, 2\bar{B}_d(t), 0\right) \\ G_4 &= \left(-\mathbf{1}_2, \begin{bmatrix} \sqrt{\kappa_1}\mathbf{a} \\ \sqrt{\gamma_1}\mathbf{a} \end{bmatrix}, \Delta_1 \mathbf{a}^\dagger \mathbf{a} + \chi_1 \mathbf{a}^\dagger \mathbf{a} \boldsymbol{\sigma}_z^1\right) \\ G_5 &= \left(\begin{bmatrix} \sqrt{\eta_l} & i\sqrt{1-\eta_l} \\ i\sqrt{1-\eta_l} & \sqrt{\eta_l} \end{bmatrix}, 0, 0\right) \\ G_6 &= \left(-\mathbf{1}_2, \begin{bmatrix} \sqrt{\kappa_2}\mathbf{b} \\ \sqrt{\gamma_2}\mathbf{b} \end{bmatrix}, \Delta_2 \mathbf{b}^\dagger \mathbf{b} + \chi_2 \mathbf{b}^\dagger \mathbf{b} \boldsymbol{\sigma}_z^2\right) \end{aligned}$$

where $\mathbf{1}_2$ is a 2×2 identity matrix and η_l is the efficiency of the circulator between the cavities (*i.e.*, $\eta_l = 1$ implies no loss). The SLH model for the entire system is formed by performing the following concatenation and series products:

$$\begin{aligned} &(G_0 \boxplus G_6^{(1)} \boxplus G_0 \boxplus G_6^{(2)}) \lhd (G_5 \boxplus G_0 \boxplus G_0) \lhd \\ &\quad (G_0 \boxplus G_4 \boxplus G_0) \lhd (G_0 \boxplus G_1 \boxplus G_2 \boxplus G_3), \end{aligned} \tag{2}$$

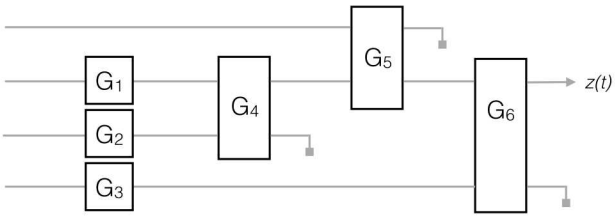

FIG. 2: SLH network decomposition of the apparatus in Fig. 1. The SLH triples (S, L, H) for each block are specified in the main text, together with the efficiencies of the relevant components. All inputs are in the vacuum state and the monitored output is $z(t)$. All other outputs are not monitored: this is indicated above by their termination.

where $G_0 = (1, 0, 0)$ is a pass-through component, and we have split the two ports of the second cavity as

$$\begin{aligned} G_6^{(1)} &= \left(-1, \sqrt{\kappa_2}\mathbf{b}, \Delta_2 \mathbf{b}^\dagger \mathbf{b} + \chi_2 \mathbf{b}^\dagger \mathbf{b} \boldsymbol{\sigma}_z^2\right) \\ G_6^{(2)} &= (-1, \sqrt{\gamma_2}\mathbf{b}, 0) \end{aligned}$$

for convenience (without this splitting, we would have to insert an routing element to swap the third and fourth signal lines after G_4 in Fig. 2). The key assumption in this SLH representation of the entire network in terms of its components is that the fields propagate with negligible time delay between the components, which we assume to be true.

Evaluating the series and concatenation products above using the rules specified in Refs. [21, 23] yields an equation of motion for the two qubits and inter-cavity modes. Adding phenomenological Markovian dephasing terms for the qubits then results in the following master equation for the cavity mode and qubit degrees of freedom:

$$\begin{aligned} \frac{\mathrm{d}\varrho}{\mathrm{d}t} &= -i[H', \varrho] + \mathcal{L}_c\varrho + \mathcal{L}_q\varrho \\ \mathcal{L}_c\varrho &= \mathcal{D}[\sqrt{\kappa_1(1-\eta_l)}\mathbf{a}] + \gamma_1\mathcal{D}[\mathbf{a}]\varrho + \gamma_2\mathcal{D}[\mathbf{b}]\varrho \\ &\quad + \mathcal{D}[-\sqrt{\kappa_1\eta_l}\mathbf{a} + \sqrt{\kappa_2}\mathbf{b}]\varrho \\ \mathcal{L}_q\varrho &= \sum_{i=1}^{2} \gamma_d^i \mathcal{D}[\boldsymbol{\sigma}_z^i]\varrho, \end{aligned} \tag{3}$$

where ϱ is the combined density matrix of the two cavity modes and qubits, γ_d^i and γ_r^i are the dephasing and relaxation rates of qubit i, and $\mathcal{D}[A]B \equiv ABA^\dagger - \frac{1}{2}A^\dagger AB - \frac{1}{2}BA^\dagger A$. The effective Hamiltonian for the coupled system is

$$\begin{aligned} H' &= H_A + H_B + H_c' + H_d' \\ H_c' &= -i\frac{\kappa_{12}}{2}(\mathbf{a}^\dagger\mathbf{b} - \mathbf{b}^\dagger\mathbf{a}), \\ H_d' &= i\left(A_d(t)\mathbf{a}^\dagger - A_d^*(t)\mathbf{a} + B_d(t)\mathbf{b}^\dagger - B_d^*(t)\mathbf{b}\right), \end{aligned} \tag{4}$$

where $\kappa_{12} = \sqrt{\kappa_1\kappa_2\eta_l}$ and the effective drives are

$$\begin{aligned} A_d(t) &= \sqrt{\gamma_1}\bar{A}_d(t) + \sqrt{\kappa_1}\bar{\xi}(t) \\ B_d(t) &= \sqrt{\gamma_2}\bar{B}_d(t) - \sqrt{\kappa_2\eta_l}\bar{\xi}(t) \end{aligned} \tag{5}$$

H_c' describes effective direct coupling of the two cavity modes due to the net field ($A_d(t)$) that is interacting with both cavities. Similarly, the effective drives for the cavity modes in H_d' are composed of the probe field and the drive fields entering the input ports. Note that the coupling in H_c' is reduced by the factor $\sqrt{\eta_l}$, due to losses in the circulator. Although the Hamiltonian form of this cavity coupling looks reversible, the irreversibility enforced by the circulator is nevertheless captured in the model when the dissipative dynamics modeled by $\mathcal{L}_c$ is also included. We shall see the effects of this explicitly below (see also Ref. [20]).

We assume that the qubits have T_1 times that are much longer than the timescales of interest for establishing entanglement by continuous joint measurement, and thus $\mathcal{L}_q$ only accounts for environmental dephasing of the qubits and not relaxation. This is a reasonable assumption for superconducting qubits, *e.g.*, [18]. Relaxation is discussed in Sec. V.

Each dissipator term in $\mathcal{L}_c$ takes into account the effect of a field irreversibly coupling out of the combined system. $\mathcal{D}[\sqrt{\kappa_1(1-\eta_l)}\mathbf{a}]$ accounts for photons lost between the two cavities, $\mathcal{D}[\mathbf{a}]$ accounts for the field emitted from the input port of cavity 1, $\mathcal{D}[\mathbf{b}]$ accounts for the field emitted from the input port of cavity 2, and $\mathcal{D}[-\sqrt{\kappa_1\eta_l}\mathbf{a} + \sqrt{\kappa_2}\mathbf{b}]$ accounts for the probe field that is reflected off the output ports of cavities 1 and 2. This final output channel is the only one that is monitored, and to complete the full model in the presence of measurement, we must describe the evolution of the system conditioned on homodyne measurement of the output field $z(t)$. The homodyne measurement is implemented by mixing the signal field with a local oscillator of fixed phase reference, ϕ, with respect to the initial phase of the probe field. This phase reference sets the measurement quadrature. The corresponding time evolution is given by [25]

$$\begin{aligned} \frac{\mathrm{d}\varrho}{\mathrm{d}t} &= -i[H', \varrho] + \mathcal{L}_c\varrho + \mathcal{L}_q\varrho + \mathcal{L}_m\varrho \\ \mathcal{L}_m\varrho &= \sqrt{\eta_\mathrm{m}}\xi(t)\mathcal{H}[e^{i\phi}(-\sqrt{\kappa_1\eta_l}\mathbf{a} + \sqrt{\kappa_2}\mathbf{b})]\varrho, \end{aligned} \tag{6}$$

where $0 < \eta_\mathrm{m} \leq 1$ is the efficiency of the measurement, ϕ defines the measurement quadrature, and $\xi(t)$ is Gaussian white noise due to the measurement. This equation is in Ito form [26] and therefore $\xi(t)dt = dW(t)$, where $dW(t)$ is a Wiener increment satisfying $E\{dW(t)\} = 0$ and $E\{dW(t)dW(s)\} = \delta(t-s)$ (E denotes expectation value). The nonlinear conditioning superoperator $\mathcal{H}$ is defined as: $\mathcal{H}[A]B \equiv AB + BA^\dagger - \mathrm{Tr}(AB + BA^\dagger)B$. Eq. (6) describes the conditioned state of the system under a homodyne measurement trace of the voltage

$$V(t) = \sqrt{\eta_\mathrm{m}}\mathrm{Re}(e^{i\phi}\langle -\sqrt{\kappa_1\eta_l}\mathbf{a} + \sqrt{\kappa_2}\mathbf{b}\rangle) + \xi(t), \tag{7}$$

where $\langle \mathbf{A} \rangle \equiv \mathrm{tr}\,(\mathbf{A}\varrho)$. Eq. (7) expresses the monitored voltage in terms the measured observable, which is a linear combination of intra-cavity field operators, a and b.

The Heisenberg equations of motion for expected values of the intra-cavity fields, under the unconditioned evolution described by Eqs. (3)-(4) are:

$$\begin{aligned}\langle \dot{\mathbf{a}} \rangle &= -i\Delta_1 \langle \mathbf{a} \rangle - i\chi_1 \langle \boldsymbol{\sigma}_z^1 \mathbf{a} \rangle - \frac{\kappa_1+\gamma_1}{2}\langle \mathbf{a} \rangle + A_d(t) \\ \langle \dot{\mathbf{b}} \rangle &= -i\Delta_2 \langle \mathbf{b} \rangle - i\chi_2 \langle \boldsymbol{\sigma}_z^2 \mathbf{b} \rangle + \kappa_{12}\langle \mathbf{a} \rangle - \frac{\kappa_2+\gamma_2}{2}\langle \mathbf{b} \rangle \\ &\quad + B_d(t).\end{aligned}$$

These evolution equations make explicit the fact that the second cavity $\langle \mathbf{b} \rangle$ is driven by the first $\langle \mathbf{a} \rangle$ but not vice-versa (*i.e.*, the irreversibility of the coupling between cavities). We assume that the driving fields $(\xi(t), A_d(t), B_d(t))$ are all coherent states and therefore these expectation values are simply the coherent state amplitudes of the intra-cavity fields. We can write these coherent state amplitudes conditioned on the qubits being in specific states as:

$$\begin{aligned}\dot{A}^{(r)} &= -i\Delta_1 A^{(r)} - (-1)^r i\chi_1 A^{(r)} - \frac{\kappa_1+\gamma_1}{2}A^{(r)} \\ &\quad + A_d(t) \\ \dot{B}^{(rs)} &= -i\Delta_2 B^{(rs)} - (-1)^s i\chi_2 B^{(rs)} - \frac{\kappa_2+\gamma_2}{2}B^{(rs)} \\ &\quad + B_d(t) + \kappa_{12}\, A^{(r)}. \end{aligned} \tag{8}$$

Here $A = \langle \mathbf{a} \rangle, B = \langle \mathbf{b} \rangle$ and the superscripts $r, s \in \{0,1\}$ indicate the conditioning on the state of the first and second qubit, respectively. The state of the second cavity is conditioned on the states of both qubits but the state of the first cavity is only conditioned on the state of the first qubit, since there is no information flowing from the second to the the first cavity. In other words, $A^{(11)} = A^{(10)} = A^{(1)}$ and $A^{(01)} = A^{(00)} = A^{(0)}$. These conditioned equations for intra-cavity amplitudes are linear and can be solved exactly (first solving for A and then for B) for any values of the driving fields. Their exact solutions will be used below.

B. Dynamics in the polaron frame

While the conditioned dynamical equation in Eq. (6) is a full model of the experiment in Ref. [18], it is difficult to simulate since it involves both qubit and cavity degrees of freedom. Therefore it is convenient to derive an effective SME for the qubit degrees of freedom only. For this purpose, in this section, we develop an SME in a polaron frame where the average state of both intra-cavity fields is displaced to the vacuum. This SME is exact within the RWA and dispersive approximation implicit in Eq. (1), and becomes easy to simulate since the intra-cavity fields are always in the vacuum state.

The polaron transformation provides a representation in which the cavity modes are effectively removed from the real time qubit dynamics. The correct transform in this two cavity case is $\varrho^P(t) = U(t)^\dagger \varrho(t) U(t)$, with

$$U(t) = \textstyle\sum_{i,j} \boldsymbol{\Pi}_{ij} D_1\left[A^{(i)}(t)\right] D_2\left[B^{(ij)}(t)\right], \tag{9}$$

where $\boldsymbol{\Pi}_{ij} = |i\rangle_1 \langle i| \otimes |j\rangle_2 \langle j|$ are projectors onto qubit states and $D_{1(2)}[X]$ is a displacement operator for cavity field 1(2) by coherent state X, *i.e.*,

$$\begin{aligned}D_1[X] &= e^{X\mathbf{a}^\dagger - X^*\mathbf{a}} \\ D_2[X] &= e^{X\mathbf{b}^\dagger - X^*\mathbf{b}}.\end{aligned}$$

For convenience, we define the following time-dependent qubit operators that depend on the intra-cavity field states:

$$\begin{aligned}\boldsymbol{\Pi}_a(t) &\equiv \boldsymbol{\Pi}_0 A^{(0)}(t) + \boldsymbol{\Pi}_1 A^{(1)}(t), \\ \boldsymbol{\Pi}_b(t) &\equiv \sum_{i,j=0,1} \boldsymbol{\Pi}_{ij} B^{(ij)}(t),\end{aligned} \tag{10}$$

where $\boldsymbol{\Pi}_0 = \boldsymbol{\Pi}_{00} + \boldsymbol{\Pi}_{01}$ and $\boldsymbol{\Pi}_1 = \boldsymbol{\Pi}_{10} + \boldsymbol{\Pi}_{11}$. These can also be viewed as operator-valued coherent states of the intra-cavity fields and arise as a consequence of the hybridization of cavity and qubit degrees of freedom induced by the polaron transform. The temporal evolution of the joint density matrix in this polaron frame is given by

$$\begin{aligned}\frac{\mathrm{d}\varrho^P}{\mathrm{d}t} &= \frac{\mathrm{d}}{\mathrm{d}t} U(t)^\dagger \varrho(t) U(t) \\ &= -i[H'^P, \varrho^P] + \mathcal{L}_c^P \varrho^P + \mathcal{L}_q^P \varrho^P + \mathcal{L}_m^P \varrho^P \\ &\quad - U^\dagger \dot{U} \varrho^P - \varrho^P \dot{U}^\dagger U,\end{aligned}$$

where $H'^P, \mathcal{L}_c^P, \mathcal{L}_q^P, \mathcal{L}_m^P$ are as defined in Eq. (3) and Eq. (6), but with each operator transformed into the polaron frame. For example, transforming the field annihilation and creation operators yields

$$\begin{aligned}U(t)^\dagger \mathbf{a} U(t) &= \mathbf{a} + \boldsymbol{\Pi}_a(t) \\ U(t)^\dagger \mathbf{b} U(t) &= \mathbf{b} + \boldsymbol{\Pi}_b(t).\end{aligned} \tag{11}$$

Performing all the polaron transformations, the SME describing conditioned evolution in this frame takes explicit form (for an unnormalized density matrix in the polaron frame):

$$\begin{aligned}\frac{\mathrm{d}\varrho^P}{\mathrm{d}t} &= -i[H_A + H_B + H_c' + H_q, \varrho^P] \\ &\quad + \mathcal{L}_c \varrho^P + \mathcal{L}_q \varrho^P + \mathcal{L}_m \varrho^P + \mathcal{L}_{mq} \varrho^P \\ &\quad + \mathbf{a}[\varrho^P, \Gamma_a \boldsymbol{\Pi}_a^\dagger + \kappa_{12} \boldsymbol{\Pi}_b^\dagger] + [\Gamma_a \boldsymbol{\Pi}_a + \kappa_{12} \boldsymbol{\Pi}_b, \varrho^P]\mathbf{a}^\dagger \\ &\quad + \mathbf{b}[\varrho^P, \Gamma_b \boldsymbol{\Pi}_b^\dagger + \kappa_{12} \boldsymbol{\Pi}_a^\dagger] + [\Gamma_b \boldsymbol{\Pi}_b + \kappa_{12} \boldsymbol{\Pi}_a, \varrho^P]\mathbf{b}^\dagger,\end{aligned} \tag{12}$$

with $\Gamma_{a/b} = \gamma_{a/b} + \kappa_{a/b}$. The new terms above are:

$$\begin{aligned}H_q &= \frac{i}{2}\left(A_d(t)\boldsymbol{\Pi}_a^\dagger - A_d^*(t)\boldsymbol{\Pi}_a + B_d(t)\boldsymbol{\Pi}_b^\dagger - B_d^*(t)\boldsymbol{\Pi}_b\right) \\ \mathcal{L}_{mq} &= \mathcal{D}[-\sqrt{\kappa_1\eta_l}\boldsymbol{\Pi}_a + \sqrt{\kappa_2}\boldsymbol{\Pi}_b] \\ &\quad + (\kappa_1(1-\eta_l) + \gamma_1)\mathcal{D}[\boldsymbol{\Pi}_a] + \gamma_2 \mathcal{D}[\boldsymbol{\Pi}_b] \\ &\quad + \sqrt{\eta_{\mathrm{m}}}\xi(t)\bar{\mathcal{H}}[e^{i\phi}(-\sqrt{\kappa_1\eta_l}\boldsymbol{\Pi}_a + \sqrt{\kappa_2}\boldsymbol{\Pi}_b)],\end{aligned} \tag{13}$$

with $\bar{\mathcal{H}}[A]B \equiv AB + BA^\dagger$. We sacrifice normalization in the following for simplicity and the normalizing factor can always be added back in by computing $\mathrm{tr}\,(\frac{\mathrm{d}\varrho^P}{\mathrm{d}t})$. In this polaron frame, the drive of the cavity modes (by A_d and B_d) is absent, because we are dynamically shifting the cavity states back to the vacuum. As a result, if the cavities are unpopulated initially, they remain unpopulated at all times. A way to see this is that all field operators annihilate ϱ^P in Eq. (12), and therefore there is no change in the states of the two cavity modes. As a consequence, all terms involving cavity modes a, b in Eq. (12) have no effect and can be dropped, which leaves an equation of motion for the qubit degrees of freedom in the polaron frame:

$$\frac{\mathrm{d}\varrho^P}{\mathrm{d}t} = -i[H_q, \varrho^P] + \mathcal{L}_q\varrho^P + \mathcal{L}_{mq}\varrho^P \tag{14}$$

The terms in H_q represent Stark shifting of the energy levels due to the interaction with the measurement tone at ω_d. The terms in $\mathcal{L}_{mq}$ (Eq. (12)) represent information about the qubits leaking out (and dephasing the qubits) with the light being carried through various outputs of the system. The last term in $\mathcal{L}_{mq}$ represents information that we gain from stochastic selection of one of the measurement outcomes.

It is important to note that Eq. (14) contains no additional approximations other than the RWA and the approximation of the Jaynes-Cummings interaction by the dispersive interaction between qubits and cavity modes. However, due to the polaronic frame transformation, as long as the cavities are initially unpopulated, this equation efficiently simulates the coupled qubit and cavity quantum degrees of freedom without the cost of keeping track of the field states in the cavity (their influence is captured by the time-dependent operators Π_a and Π_b in Eq. (14)).

C. Transforming back to the lab frame

In order to make predictions with respect to the lab frame, we transform the density matrix that results from Eq. (14) back into the lab frame. We can achieve this by first noting that the state of the system at an arbitrary time in the polaron frame takes the form:

$$\varrho^P(t) = \sum_{ijkl} r_{ijkl}(t)\,|ij\rangle\langle kl| \otimes |00\rangle\langle 00|\,. \tag{15}$$

The $ijkl$ indices run over $\{0,1\}$ and index the qubit states. The second term in the tensor product, $|00\rangle\langle 00|$, is the state of the intra-cavity fields. Both modes are in the vacuum state since in the polaron frame the cavities remain unoccupied. Then the state of the entire system in the lab frame is given by $\varrho(t) = U(t)\varrho^P(t)U^\dagger(t)$, and the state of the qubits in the lab frame is given by

$$\rho(t) = \mathrm{tr}_{\,c1,c2}\left(U(t)\varrho^P(t)U^\dagger(t)\right), \tag{16}$$

where the trace is over both cavity modes. If we let

$$\rho(t) = \sum_{ijkl} \rho_{ijkl}(t)\,|ij\rangle\langle kl|\,, \tag{17}$$

we can compute the relation between $\rho_{ijkl}(t)$ and $r_{ijkl}(t)$, using the definition of the polaron transform in Eq. (9) and computing Eq. (16). Doing this tells us that the diagonal elements remain unchanged,

$$\rho_{ijij}(t) = r_{ijij}(t),$$

but, the off-diagonal components are modified as

$$\rho_{ijkl}(t) = r_{ijkl}(t)e^{\Upsilon_{ijkl}(t)}, \tag{18}$$

where the compensation factor is

$$\begin{aligned}\Upsilon_{ijkl}(t) &= i\mathrm{Im}\{A^{(k)*}A^{(i)}\} + i\mathrm{Im}\{B^{(kl)*}B^{(ij)}\} \\ &\quad -\frac{|A^{(i)} - A^{(k)}|^2}{2} - \frac{|B^{(ij)} - B^{(kl)}|^2}{2}.\end{aligned} \tag{19}$$

These relations suggest that an efficient method for simulation of the system in the lab frame is to compute the time dynamics in the polaron frame according to Eq. (14) (giving $r_{ijkl}(t)$), and then at each time, to compute the compensation to the off-diagonal elements given by Eq. (18) to get the reduced state of the qubits in the lab frame.

D. Reduced equation of motion for the qubits

Another approach for obtaining the state of the two qubits at any time is to formulate an equation of motion for just the qubit degrees of freedom in the lab frame. We begin with the expression for a general two qubit state in the lab frame given in Eq. (17). Taking the time derivative of this state yields:

$$\frac{\mathrm{d}}{\mathrm{d}t}\rho_{ijij}(t) = \frac{\mathrm{d}}{\mathrm{d}t}r_{ijij}(t)$$

for the diagonal elements, and

$$\frac{\mathrm{d}}{\mathrm{d}t}\rho_{ijkl} = \left(\frac{\mathrm{d}}{\mathrm{d}t}r_{ijkl}(t)\right)e^{\Upsilon_{ijkl}(t)} + \rho_{ijkl}\left(\frac{\mathrm{d}}{\mathrm{d}t}\Upsilon_{ijkl}(t)\right) \tag{20}$$

The time derivative of r_{ijkl} is determined by the polaron frame SME in Eq. (14), and the time derivative of the compensation factor can easily be found from its definition in Eq. (19) and the equation of motion for the conditional intra-cavity fields, Eq. (8). This is similar to the approach taken in Ref. [22] for a single cavity setup.

Computing the derivatives required in Eq. (20) and canceling common factors yields the following equations of motion for the on- and off-diagonal components of the

(unnormalized) lab frame qubit density matrix:

$$\begin{aligned}\dot{\rho}_{ijkl} &= \rho_{ijkl}\Big[i2\chi_1(1-\delta_{ik})\left((-1)^i A^{(k)*}A^{(i)}\right) \\ &\quad + i2\chi_2(1-\delta_{jl})\left((-1)^j B^{(kl)*}B^{(ij)}\right) \\ &\quad - 2\gamma_d^1(1-\delta_{ik}) - 2\gamma_d^2(1-\delta_{jl}) \\ &\quad + \sqrt{\eta_{\rm m}}\xi(t)\{\tilde{B}^{(ij)} + \tilde{B}^{(kl)*}\}\Big], \qquad (21)\end{aligned}$$

with $\tilde{B}^{(ij)} \equiv e^{i\phi}(-\sqrt{\kappa_1\eta_l}A^{(i)} + \sqrt{\kappa_2}B^{(ij)})$. This evolution can also be represented in matrix form (for an unnormalized qubit density matrix) as:

$$\begin{aligned}\frac{{\rm d}\rho}{{\rm d}t} &= \sum_{ijkl} a_{ijkl}(t)\mathbf{\Pi}_{ij}\rho(t)\mathbf{\Pi}_{kl} + \sum_{i=1}^{2}\gamma_d^i\mathcal{D}[\sigma_z^i]\rho \\ &\quad + \sqrt{\eta_{\rm m}}\xi(t)\bar{\mathcal{H}}[e^{i\phi}(-\sqrt{\kappa_1\eta_l}\mathbf{\Pi}_a + \sqrt{\kappa_2}\mathbf{\Pi}_b)], \qquad (22)\end{aligned}$$

with

$$\begin{aligned}a_{ijkl}(t) &\equiv i2\chi_1(1-\delta_{ik})\left((-1)^i A^{(k)*}A^{(i)}\right) \\ &\quad + i2\chi_2(1-\delta_{jl})\left((-1)^j B^{(kl)*}B^{(ij)}\right)\end{aligned}$$

Eq. (22) should be treated with care because although it looks like an SME with deterministic component in Lindblad form, it is not strictly in Lindblad form since the coefficient matrix defined by $a_{ijkl}(t)$ is not necessarily positive. Hence this equation can result in non-Markovian evolution of the qubit, which is physically a result of tracing out the intracavity degrees of freedom that are strongly entangled with the qubit states. Therefore physical interpretations of Eq. (22) are difficult, but it generates the correct qubit evolution in the lab frame, and presents an alternative to simulating the qubit evolution in the polaron frame according to Eq. (14).

E. Simulation in different frames

The derivation of a reduced equation of motion for the qubit degrees of freedom only under the continuous weak measurement allow us to identify the exact qubit observable being monitored by the sequential probe: $\mathrm{Re}\{e^{i\phi}\langle -\sqrt{\kappa_1\eta_l}\mathbf{\Pi}_a + \sqrt{\kappa_2}\mathbf{\Pi}_b\rangle\}$.

Let us examine this observable under ideal conditions, where there are no losses and the two sets of cavities and qubits are identical; *i.e.*, $\eta_l = 1, \kappa_1 = \kappa_2 = \kappa, \chi_1 = \chi_2 = \chi, \Delta_1 = \Delta_2 = 0$. In this ideal scenario, there is no need to apply compensating tones through the input ports of the cavities (as we shall see below), and so we shall additionally set $\gamma_1 = \gamma_2 = 0$, whereby $A_d(t) = \sqrt{\kappa_1}\bar{\xi}(t)$ and $B_d(t) = -A_d(t)$.

In this subsection we present an example time evolution that illustrates the points raised in the derivation above of equations of motion for the qubits in the lab frame. We again assume no loss and identical cavitites, with simulation parameters: $\eta_l = 1, \kappa_1 = \kappa_2 =$ 14MHz, $\chi_1 = \chi_2 = 1$MHz, $\Delta_1 = \Delta_2 = 0$ and $\gamma_1 = \gamma_2 = 0$. Fig. 3 shows the ρ_{0110} off-diagonal component of the qubit density matrix under a particular measurement trajectory, simulated using the three dynamical equations derived above: *polaron* Eq. (14), *compensated polaron* Eq. (14) with Eq. (18), and *reduced* Eq. (22). The top panel of the figure also shows the measurement pulse $A_d(t)$ that produced the trajectory. As this figure shows, and as expected from the derivation in II D, the compensated polaron and the reduced evolution equations produce exactly the same results. However, they both differ from the polaron frame evolution equation unless the photon population of both cavities is zero. Finally, another interesting feature is revival of coherence produced by the two lab frame SMEs (polaron compensated and reduced) between 2 and 2.5μs, after the pulse has decayed to zero. This is evidence of the non-Markovian nature of the evolution equations due to the elimination of the strongly entangled cavity states. Note that a similar effect should be expected even in the single cavity case [22], and even in this case the stated lab "dephasing rate" would be expected to be non-Markovian.

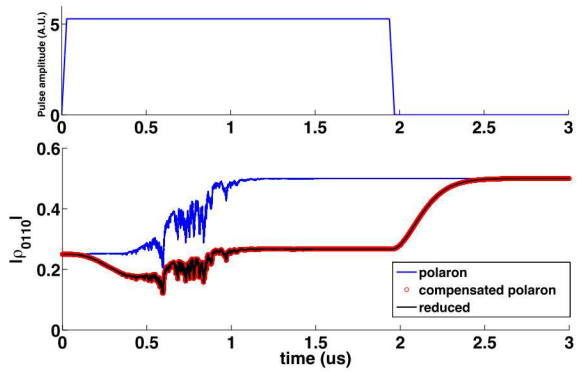

FIG. 3: (Color online) A sample trajectory of $|\rho_{0110}(t)|$, the absolute value of an off-diagonal qubit density matrix element simulated using the three dynamical equations derived in Sec. II B, II C and II D. The parameters used in the simulations are described in the main text. The top panel of the figure also shows the measurement pulse $A_d(t)$.

III. CONDITIONS FOR GENERATING ENTANGLEMENT

In this section, we demonstrate how the sequential coherent probe and subsequent homodyne detection can result in a half-parity measurement of the qubits, which can probabilistically entangle the qubits. In particular, we will specify in Sec. III D how the parameters that can be controlled *in-situ* (*e.g.*, frequency, amplitude and phase of drive tones $A_d(t), B_d(t)$) can be tuned to generate entanglement between the qubits even whenever the system parameters are not ideal.

The key fact that the probabilistic entanglement

scheme relies on is that under the half-parity measurement, the states $|01\rangle$ and $|10\rangle$ are indistinguishable. Then starting in the initial separable state

$$|\Psi_0\rangle = \frac{1}{2}(|00\rangle + |01\rangle + |10\rangle + |11\rangle\,, \tag{23}$$

for entanglement to be generated by measurement the initial coherence between $|01\rangle$ and $|10\rangle$ must be preserved (or at least not decay substantially). For this to happen, the indistinguishability between these states must be maintained at all times, i.e., it is not sufficient that the measurement voltage be the same for both states at the final time. In this section, we will examine this condition more carefully.

As derived in the previous section, the homodyne measurement effectively observes the qubit observable: $\mathrm{Re}\{e^{i\phi}\langle -\sqrt{\kappa_1\eta_l}\mathbf{\Pi}_a + \sqrt{\kappa_2}\mathbf{\Pi}_b\rangle\}$. For indistinguishability we require that this quantity is equal when the qubit is in state $|01\rangle$ or $|10\rangle$. Equivalently, we require that for all t,

$$\begin{aligned} &\mathrm{tr}\left[(-\sqrt{\kappa_1\eta_l}\mathbf{\Pi}_a(t) + \sqrt{\kappa_2}\mathbf{\Pi}_b(t))\,|01\rangle\langle 01|\,\right] \\ &= \mathrm{tr}\left[(-\sqrt{\kappa_1\eta_l}\mathbf{\Pi}_a(t) + \sqrt{\kappa_2}\mathbf{\Pi}_b(t))\,|10\rangle\langle 10|\,\right] \\ \Rightarrow\quad &\mathrm{tr}\left[(-\sqrt{\kappa_1\eta_l}\mathbf{\Pi}_a(t) + \sqrt{\kappa_2}\mathbf{\Pi}_b(t))\mathbf{\Pi}^{\perp}_{\mathrm{DFS}}\right] = 0, \end{aligned} \tag{24}$$

where $\mathbf{\Pi}^{\perp}_{\mathrm{DFS}} = |01\rangle\langle 10| - |10\rangle\langle 10|$, is a projector orthogonal to the subspace that we desire to be decoherence-free (or more accurately, measurement-induced dephasing free). We note that derivatives (with respect to time) of the expression on the left must also be zero ideally.

To obtain a prescription for tuning the experimental parameters (specifically the compensating field, $B_d(t)$), we substitute the value of $\mathbf{\Pi}_b(t)$ given by the equations of motion (8) and (10) into Eq. (24), obtaining

$$\begin{aligned} \mathrm{tr}\Bigg[\Bigg(&(\kappa_{12}\mathbf{\Pi}_a + B_d - \dot{\mathbf{\Pi}}_{\mathbf{b}})\frac{\tilde{\kappa}_2 - i\chi_2\boldsymbol{\sigma}_z^2}{\tilde{\kappa_2}^2 + \chi_2{}^2} \\ &- \frac{\sqrt{\kappa_1\eta_l}}{\sqrt{\kappa_2}}\mathbf{\Pi}_a\Bigg)\mathbf{\Pi}^{\perp}_{\mathrm{DFS}}\Bigg] = 0. \end{aligned} \tag{25}$$

This is a general dynamical condition for the parameters in the system to meet as the system evolves. However, it is a self-consistency equation for B_d because the operator $\dot{\Pi}_b$ depends implicitly on B_d. In the following, we discuss simple solutions for three limiting, but physically relevant, regimes, as well as the more complex general solution that requires pulse-shaping.

A. Adiabatic regime

In the regime where the probe fields vary very slowly or not at all (*e.g.*, steady-state or continuous-wave measurement) it is sufficient to solve for the instantaneous eigenstates of the evolution operator. Physically, this is the limit where $\dot{A}_d, \dot{B}_d \ll \kappa_1, \kappa_2$. We can approximate $A_d(t)$ and $B_d(t)$ as constant fields for short times and solve for the "adiabatic values" of the hybridized field operators by setting the derivatives in equations Eq. (8) to zero. This was done for the special case of identical cavities and no loss in Eq. (**??**), but the general solution for $\mathbf{\Pi}_a$ is

$$\mathbf{\Pi}_a^{adb}(t) = \frac{A_d(t)(\tilde{\kappa}_1 - i\chi_1\boldsymbol{\sigma}_z^1)}{\tilde{\kappa_1}^2 + \chi_1{}^2} \tag{26}$$

$$\mathbf{\Pi}_b^{adb}(t) = \frac{(\kappa_{12}\mathbf{\Pi}_a^{adb}(t) + B_d(t))(\tilde{\kappa}_2 - i\chi_2\boldsymbol{\sigma}_z^2)}{\tilde{\kappa_2}^2 + \chi_2{}^2}, \tag{27}$$

with $\tilde{\kappa}_i = \kappa_i/2 + \gamma_i/2 + i\Delta_i$. Substituting $\Pi_a \to \Pi_a^{ad}$ in Eq. (25) and dropping the $\dot{\mathbf{\Pi}}_{\mathbf{b}}$ term (since this is small in this regime), and then solving for $B_d(t)$ in terms of the other quantities yields

$$B_d^{adb}(t) = \kappa_{12}A_d(t)\frac{(\chi_1\tilde{\kappa}_2 - \chi_2\tilde{\kappa}_1) - (\tilde{\kappa_2}^2 + \chi_2{}^2)\chi_1/\kappa_2}{\chi_2(\tilde{\kappa_1}^2 + \chi_1{}^2)}. \tag{28}$$

This equation defines the value of the compensation field driving the second cavity, $\bar{B}_d(t)$, that acheives indistinguishability of the states $|01\rangle$ and $|10\rangle$. Equivalently, another approach to achieving indistinguishability, without using the compensating drive (i.e. $\bar{B}_d(t) = 0$), is to tune the frequency of the drive A_d. This gives a condition on $\Delta_1(t)$ in order to meet Eq. (28), and was the approach chosen in Ref. [18] due to its simplicity, though it is only possible for certain parameter ranges. In both cases, condition Eq. (28) can be met by tuning the parameter(s) *in-situ* to obtain the same measurement statistics when the qubits are in states $|01\rangle$ and $|10\rangle$.

B. Large cavity-decay regime

The adiabatic approach works best in the limit of very large cavity decay rates κ_i, where the transient-evolution time periods leading up to and following the steady-state are short enough enough to be entirely negligible. In such a case, we can instead simply use square pulses for the measurement tone A_d, as well as for the compensation via auxiliary measurement drive B_d or frequency calibration Δ_1.

Additionally, if we assume $\kappa_1, \kappa_2 \gg \chi_1, \chi_2$, Eq. (28) simplifies to

$$B_d^{uni}(t) = -\sqrt{\frac{\eta\kappa_1}{\kappa_2}}A_d(t)\frac{(\tilde{\kappa}_2(\Delta_2(t) - \kappa_2/2)\chi_1 + \tilde{\kappa}_1\kappa_2\chi_2/2)}{\tilde{\kappa_1}^2\chi_2}. \tag{29}$$

where the time dependence is left in for generality but is not typically needed. This simplicity of this approach is of practical utility and was used in Ref. [18]. Note however, that the cavity decay rates can only be increased up to a certain point imposed by physical constraints and so a small transient error will remain.

Fig. 4 shows the degradation of coherence as a result of transient populations in the cavities (that is using Eq. (28) only for calibration). This figure shows

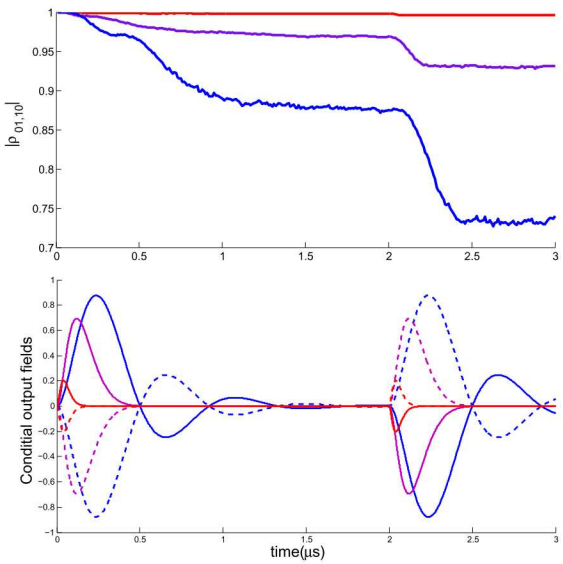

FIG. 4: (Color online) Coherence between the $|01\rangle$ and $|10\rangle$ states (top) and field amplitudes for $|01\rangle$ (solid) and $|10\rangle$ (dashed) (bottom) for different values of the cavity decay rate κ_1. The different lines are $\kappa_1 = \{3.9, 4.5, 5.1, 5.8, 6.4\}$MHz , with $\kappa_2/2\pi = 0.9\kappa_1$. Other parameters are listed in the main text.

the decay of the off-diagonal element $|\rho_{0110}|$ while the measurement tone is applied for various values of cavity transmittivity. The parameters are the same as in Fig. 3, except with $\chi_1/2\pi = 1.2$MHz, κ_1 takes on the values $\{2\pi, 5\times 2\pi, 17\times 2\pi\}$, with $\kappa_2{=}\kappa_1 + 2.5\times 2\pi$. With $A_d = \sqrt{0.9\kappa_1}/2\pi$ and using the same pulse shape as in Fig. 3, the total needed measurement time is kept approximately fixed. The initial state is $|\Psi_0\rangle$, and the dynamical equation is given by Eq. (14), averaged over 1500 trajectories. The bottom panel of the figure also shows the conditional output fields corresponding to the qubits being in state $|01\rangle$ and $|10\rangle$, $\mathrm{Re}\{\tilde{B}^{(01)}\}$ and $\mathrm{Re}\{\tilde{B}^{(10)}\}$ (i.e. ϕ=0). As expected, since the simplified compensation prescribed by Eq. (28) (or Eq. (29) for the larger values of κ) is utilized the qubit states are distinguishable by the output fields during the pulse transients, and the greater this distinguishability, the greater the loss of coherence. The point here is that with larger decay factors, these transients become smaller. Thus, a cavity decay rate of $\kappa = 3.9$MHz causes 40% loss of coherence, while in contrast $\kappa = 6.4$MHz causes negligible loss.

C. Ideal system parameter regime

In the ideal case, when the transmission is lossless (η_l=1) and the cavities are identical ($\kappa_1{=}\kappa_2$, $\chi_1{=}\chi_2$, $\Delta_1{=}\Delta_2$,$\gamma_1{=}\gamma_2$), Eq. (28) reduces to

$$B_d(t) = -A_d(t). \tag{30}$$

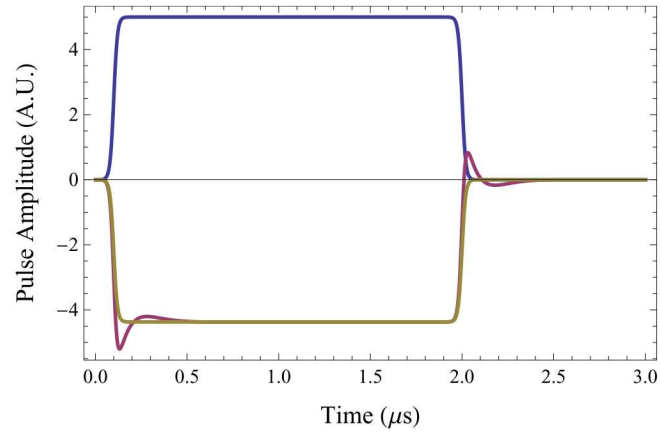

FIG. 5: (Color online) Example of a measurement pulse and compensation. The solid blue line is the pulse $A_d(t)$. The compensation pulse $B_d(t)$ is shown in dotted orange when the adiabatic approximation is used (Eq. (28)) while the dotted red shows the exact solution given by Eq. (32). The parameters are the same as in Fig. 3 but with κ_1=3.9MHz and κ_2=3.5MHz.

This is equivalent to driving only using the reflection mode of the cavities such that the compensations fields are not needed ($\bar{A}_d(t){=}\bar{B}_d(t){=}0$ in Eq. (5)). Alternatively, the same result is obtained if the cavities are driven only through their input ports such that $\bar{\xi}(t){=}0$ and $\sqrt{\gamma_2}\bar{B}_d(t) = 2\sqrt{\kappa_1}\bar{A}_d(t)$.

In both these cases, there is a benefit that for all parameter values, the transients will exactly cancel and the indistinguishability condition (Eq. (24)) will be met at all times. This is apparent in Sec. II E and Fig. 3 where we see that for identical parameters the coherence of the entangled state does not decrease at all during the periods of transient evolution of the cavities.

The reason for this can easily be understood by looking at the equations of motion for the cavities (Eq. (8)) in the limit of identical cavity parameters and using Eq. (30). The qubit quantity being measured becomes proportional to $\mathrm{Re}\{e^{i\phi}(\mathbf{\Pi}_b(t) - \mathbf{\Pi}_a(t))\}$, and taking the second derivative of Eq. (24) yields the following condition on the indistinguishability:

$$\begin{aligned} &\mathrm{tr}\ \left[\left(\ddot{\mathbf{\Pi}}_b(t) - \ddot{\mathbf{\Pi}}_a(t)\right)\mathbf{\Pi}^{\perp}_{\mathrm{DFS}}\right] = 0 \\ \Rightarrow\ &\mathrm{tr}\ \left[\left(\chi^2(\dot{\mathbf{\Pi}}_b(t) - \dot{\mathbf{\Pi}}_a(t)) - \frac{\kappa^2}{4}(\mathbf{\Pi}_b(t) - \mathbf{\Pi}_a(t))\right)\mathbf{\Pi}^{\perp}_{\mathrm{DFS}}\right] = 0. \end{aligned}$$

From the second line it is clear that if the condition is met initially, it is met also at all later times. This motivates attempting to obtain parameters that are as similar as possible between the two cavities.

D. General dynamic condition

To fully eliminate the effect of transients, shaping of the measurement pulses is necessary. In particular, the

compensation field $B_d(t)$ should be shaped to ensure that the indistinguishability condition, Eq. (24), is met at all times.

In the following, we leave $A_d(t)$ unchanged (thus fully specifying $\mathbf{\Pi}_a(t)$) and shape $B_d(t) = B_d^{ad}(t) + \Delta B_d(t)$ so that it enforces the entanglement criteria at all times. To derive the result, we supplement Eq. (24) with its first and second derivative, which must also hold, and relate the derivatives of $\mathbf{\Pi}_b(t)$ using Eq. (8) and its first derivative.

The second derivative of Eq. (24) gives, upon inserting the derivative of Eq. (8),

$$\mathrm{tr}\left[\left(\sqrt{\frac{\kappa_1\eta_l}{\kappa_2}}\ddot{\mathbf{\Pi}}_a - \kappa_{12}\dot{\mathbf{\Pi}}_a + (\tilde{\kappa}_2 + i\chi_2\boldsymbol{\sigma}_z^2)\dot{\mathbf{\Pi}}_b\right)\mathbf{\Pi}_{\mathrm{DFS}}^{\perp}\right] = 0,$$

while the first derivative of Eq. (24) gives simply

$$2\tilde{\kappa}_2\mathrm{tr}\left[\left(\sqrt{\frac{\kappa_1\eta_l}{\kappa_2}}\dot{\mathbf{\Pi}}_a - \dot{\mathbf{\Pi}}_b\right)\mathbf{\Pi}_{\mathrm{DFS}}^{\perp}\right] = 0, \qquad (31)$$

Adding these to $(\tilde{\kappa}_2^2 + \chi_2^2)$ times Eq. (25) yields

$$\Delta B_d(t) = \frac{-i\kappa_{12}}{2\chi_2}\mathrm{tr}\left[\left((\tilde{\kappa}_2 - i\chi_2\boldsymbol{\sigma}_z^2 - \frac{\tilde{\kappa_2}^2 + \chi_2{}^2}{\kappa_2})\Delta\mathbf{\Pi}_a + (1 - 2\frac{\tilde{\kappa}_2}{\kappa_2})\dot{\mathbf{\Pi}}_a - \frac{1}{\kappa_2}\ddot{\mathbf{\Pi}}_a\right)\mathbf{\Pi}_{\mathrm{DFS}}^{\perp}\right], \qquad (32)$$

which fully specifies the shape parameterization of the compensation field, where $\Delta\mathbf{\Pi}_a(t) = \mathbf{\Pi}_a(t) - \mathbf{\Pi}_a^{adb}(t)$. Note also that the derivative of $\mathbf{\Pi}_a$ is proportional to its deviation from the adiabatic value ($\dot{\mathbf{\Pi}}_a(t) = (\tilde{\kappa}_1 - i\chi_1\boldsymbol{\sigma}_z^1)\Delta\mathbf{\Pi}_a(t)$). Thus, in the limit of small dispersive coupling ($\kappa \gg \chi$), we have that the change in the compensation field relative to its adiabatic value is simply proportional to the first cavity's average deviation from its adiabatic value.

This is shown in Fig. 5 where the solid blue line is the pulse $A_d(t)$. The compensation pulse $B_d(t)$ is shown in dotted orange when the adiabatic approximation is used (Eq. (28)), while the dashed red line shows the exact solution given by Eq. (32). The parameters used for this simulation are specified in section IV, with the only difference that κ_1=3.9MHz and κ_2=3.5MHz here. The compensation field is seen to change only slightly during the transient periods and is otherwise very similar to the original pulse.

IV. RESULTS FOR LOSSY TRANSMISSION

In this section we describe the results from simulating the dynamics of the system in Fig. 1 using the theoretical description developed in section II and experimentally realistic parameters. We use the polaron frame reduced master equation, Eq. (14), with a large number of random realizations of $dW(t)$ (60000 trajectories). The choice of this frame is for computational efficiency since we will only study observable values at the end of a measurement, when the cavities are unpopulated, and hence the polaron and lab frames coincide. For these simulations we use the parameters $\chi_1 = 1.2$MHz, $\chi_2 = 1.0$MHz, $\kappa_1 = 18$MHz, $\kappa_2 = 16$MHz, $\Delta_1 = \Delta_2 = 0$, $\gamma_1 = \kappa_1/20$,$\gamma_2 = \kappa_2/20$, and $\sqrt{\gamma_1}A_d(t) = 10$MHz. These parameters are representative of the parameter regime currently accessible in superconducting cavity-QED architectures [18]. The compensation field, $B_d(t)$, is chosen according to Eq. (28) to ensure the distinguishability of the states in the single-excitation subspace, except for during transients (we made this choice instead of compensation according to Eq. (32) since this full compensation requires complex pulse shaping and hence is less practical).

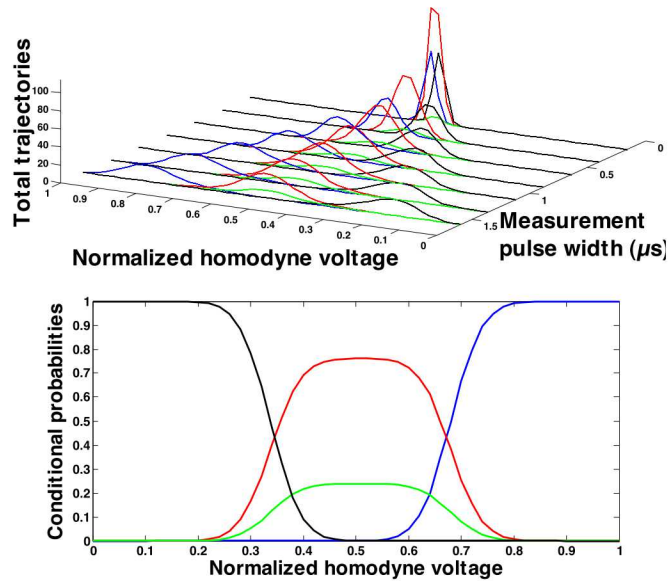

FIG. 6: (Color online) Distribution of qubit state populations (over 60000 trajectory simulations) as a function of normalized homodyne voltage and measurement pulse width. Black represents $|00\rangle$ population, blue $|11\rangle$, red $|01\rangle+|10\rangle$ and green represents $|01\rangle - |10\rangle$. The top panel plots relative population expectations conditioned on the initial state, Eq. 23. The bottom panel plots normalized populations conditioned on the measurement voltage value from the x-axis. The bottom plot is essentially a slice of the top panel taken at a measurement pulse duration of 1μs. Simulation parameters are specified in section IV.

In a pulsed measurement setup the width of the measurement pulse dictates how resolved the qubit states become. In Fig. 6 we show the how the state populations are distributed as a function of the (normalized) homodyne voltage and the measurement pulse width over the 60000 trajectories that were simulated. In the bottom panel, which is a slice at measurement pulse width of 1μs. We see that for short pulse widths little information is carried out of the cavities, and all qubit states are equally likely (low SNR). For all pulse widths, due to the

compensation pulse we see that the $|01\rangle$ and $|10\rangle$ states are indistinguishable by the homodyne voltage value. In addition, beyond pulse widths of about 1μs, homodyne voltages near the center predict that primarily the single excitation subspace is populated. The presence of the $\frac{1}{\sqrt{2}}|01\rangle + |10\rangle$ state indicates that the indistinguishability condition has been satisfied between $|01\rangle$ and $|10\rangle$. However, even if this is the case, other sources of dephasing can result in a mixed state with no entanglement even when the homodyne voltage is near its center value. For this reason we also plot the population of the state $\frac{1}{\sqrt{2}}(|01\rangle - |10\rangle)$ that would indicate a mixture with no entanglement and we see that this is not the case for measurement pulse widths $\sim 1\mu$s, but that the population of this antisymmetric state increases as the measurement pulse width increases as a result of intrinsic dephasing becoming significant at longer times. Therefore, this plot shows the tradeoff between achieving high SNR with long measurement pulses and compensation for indistinguishability, but avoiding intrinsic dephasing at longer timescales.

To explore the influence of the two primary detrimental effects to achieving entanglement between qubits in separate cavities, namely loss between cavities (η_l) and measurement inefficiency ($1-\eta_{\rm m}$), we quantify the maximum achievable entanglement (as quantified by concurrence [27]) for a range of these parameters in Fig. 7. The maximal achievable concurrence (maximized over the measurement pulse width, over a range $0.1-4\mu$s) is plotted as a function of both loss of photons between the cavities (in dB) and measurement efficiency. Not surprisingly, losses between the cavities leads to dephasing of the first qubit and hence degrades the entangled state formed with the second qubit. At the same time, decreased efficiency does not by itself lead to lower coherence, but instead necessitates longer measurement pulse widths or larger probe field amplitudes (*i.e.*, use more photons to obtain the same amount of information). However, low efficiency combined with loss between cavities is detrimental because even though one can increase the number of photons used to probe the qubits, this results in more photons being lost between cavities and thus greater dephasing. Thus, a combination of low efficiency and large loss between cavities is most unfavorable.

V. POPULATION TRANSFER IN THE POLARON FRAME

The reduced model developed above and the analysis that followed are only valid when there are no terms in the original master equation Eq. (3) that do not commute with the polaron transformation. Thus, if we choose to use the reduced model (to gain computational efficiency) we must be careful that effects such as qubit relaxation and qubit driving are taken into account. That is we

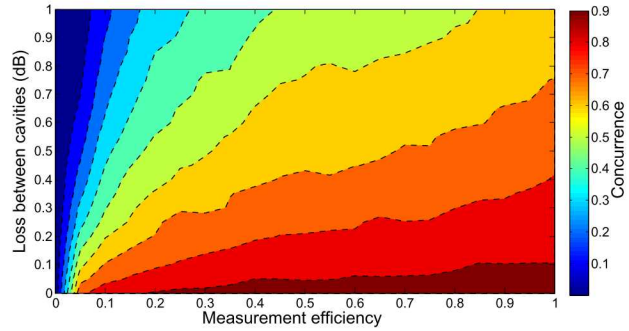

FIG. 7: (Color online) Maximum concurrence versus measurement efficiency ($\eta_{\rm m}$) and photon loss in the channel between the cavities ($1-\eta_l$, in dB). Simulation parameters are specified in section IV. Entanglement maximum is calculated by propagating the simulation for different measurement pulse widths and selecting the maximal concurrence achieved for the given parameters.

consider the more general cases where

$$H_q' = H_q + \Omega_1(t)\boldsymbol{\sigma}_x^{(1)} + \Omega_2(t)\boldsymbol{\sigma}_x^{(2)}, \tag{33}$$

$$\mathcal{L}_q\varrho = \sum_{i=1}^{2}\left(\gamma_d^i\mathcal{D}[\boldsymbol{\sigma}_z^i]\varrho + \gamma_r^i\mathcal{D}[\boldsymbol{\sigma}_-^i]\varrho\right), \tag{34}$$

For applications such as qubit measurement in the presence of relaxation, qubit manipulation during continuous-wave measurement, and feeback-control applications, it is typically expected however that the amplitude of such effects will be small and can be treated perturbatively.

The hybradization of the qubits and cavities will result in the cavity also being driven. That is, the two-cavity polaron transformation, Eq. (9) tilts the $\sigma_x^{(i)}$ axes as

$$\begin{aligned}(\boldsymbol{\sigma}_-^{(1)})^P &= D_2\left[\boldsymbol{\Pi}_b\right]D_1\left[\boldsymbol{\Pi}_a\right]\boldsymbol{\sigma}_-^{(1)}D_1^\dagger\left[\boldsymbol{\Pi}_a\right]D_2^\dagger\left[\boldsymbol{\Pi}_b\right]\\ (\boldsymbol{\sigma}_-^{(2)})^P &= D_2\left[\boldsymbol{\Pi}_b\right]\boldsymbol{\sigma}_-^{(2)}D_2^\dagger\left[\boldsymbol{\Pi}_b\right].\end{aligned} \tag{35}$$

For simplicity, we consider adiabatic measurement. Using the parameterization of Eq. (27) we obtain to first order in $A_d\chi/\kappa^2$

$$\begin{aligned}(\boldsymbol{\sigma}_-^{(1)})^P &= \boldsymbol{\sigma}_-^{(1)}(1 - A_d(1+\zeta_2)\mu_1\mathbf{a} + A_d^*(1+\zeta_2^*)\mu_1^*\mathbf{a}^\dagger),\\ (\boldsymbol{\sigma}_-^{(2)})^P &= \boldsymbol{\sigma}_-^{(2)}(1 - (B_d + A_d\zeta_1)\mu_2\mathbf{a} + (B_d^* + A_d^*\zeta_1^*)\mu_2^*\mathbf{a}^\dagger),\end{aligned} \tag{36}$$

where $\mu_i = \chi_i/((\kappa_i/2 + i\Delta_i)^2 + \chi_i^2)$ an $\zeta_i = \kappa_{12}(\kappa_i/2 + i\Delta_i)/((\kappa_i/2 + i\Delta_i)^2 + \chi_i^2)$. Thus, we see that, in the polaronic frame, qubit driving and relaxation will also lead to sideband transitions involving the cavity.

For qubit driving, we note that these will be small when $\Omega A_d\chi \ll \kappa^3$ where Ω is the Rabi frequency. In such a limit, the off-resonant sidebands will mainly result in

shifting the energies of the qubit and cavity. The qubit equation can be rewritten as

$$H_q' = H_q \; + \; \Omega_1 \boldsymbol{\sigma}_x^{(1)} - 2{\lambda_1}^2 \frac{2{\Omega_1}^2 \boldsymbol{\sigma}_x^{(1)} + \Omega_1 \chi_1 \boldsymbol{\sigma}_z^{(1)}}{(\kappa_1/2 + i\Delta_1)^2 - {\chi_1}^2 - 4{\Omega_1}^2} + \; \Omega_2 \boldsymbol{\sigma}_x^{(2)} - 2{\lambda_2}^2 \frac{2{\Omega_2}^2 \boldsymbol{\sigma}_x^{(2)} + \Omega_2 \chi_2 \boldsymbol{\sigma}_z^{(2)}}{(\kappa_2/2 + i\Delta_2)^2 - {\chi_2}^2 - 4{\Omega_2}^2} \tag{37}$$

with $\lambda_1 = A_d \mu_1 (1 + \zeta_2)$, $\lambda_2 = B_d \mu_2 + A_d \mu_2 \zeta_1$, and which can be used with the effective qubits-only master equation, Eq. (14). However, effects outside of the qubit subspace will also remain, such as sideband heating of the cavity. Much like the relaxation operators, it seems difficult to decouple the qubit and cavity dynamics completely, as they form a complex non-Markovian environment, which is out of the scope of this article. Nonetheless, it is evident from Eq. (37) that the same control pulses imposed in the frames corresponding to the laboratory and polaron frames will result in different angles of rotation and will only agree in the limit of zero photons in the cavities. In the steady state and dispersive limit, the axes of rotation are constant and it is then easy to calibrate the X and Y rotation angles resulting from a given control pulse in either frame.

The dressed frame also effects the dynamics of population transfer. It results in the pinning of population due to measurement thereby suppressing the coherent dynamics. This is known as the quantum Zeno effect [28]. For qubit manipulation, we are most interested in the weak limit of this effect, where the measurement timescale is long (weak pinning) relative to the qubit driving. Fig. 8 shows how the fidelities of a $\pi/2$ gate vary as the measurement strength is increased, for two different gate times (a 10ns and 40 ns pulse). We see that the fidelity decreases slower with the shorter (higher energy) pulse, consistent with the axis of rotation being less affected by the measurement. Increasing the driving strength can also reduce this effect, though spectral crowding issues such as the cavity sideband driving illustrated above and other experimental constraints will place a limit on how hard one can drive.

VI. DISCUSSION AND CONCLUSIONS

We have derived a framework for describing joint dispersive measurement of qubits in separate cavities. The description shows how populations of the qubit levels evolve diffusively as a function of a cascaded measurement, and how calibrating the amplitude or frequency of the field(s) enables preservation of the coherence between the single-excitation states during the measurement. The static and dynamic entanglement conditions derived in the energy basis of the system give a simple prescription for ensuring this indistinguishability at all times. Moreover, the simulations show the tolerance of the entanglement to imperfections in the measurement and loss channels along the probe field path. Finally, single trajectory analysis and simulations show that the cascaded probe field provides a non-Markovian environment resulting in suppression and revival of coherence of the bare laboratory qubit states.

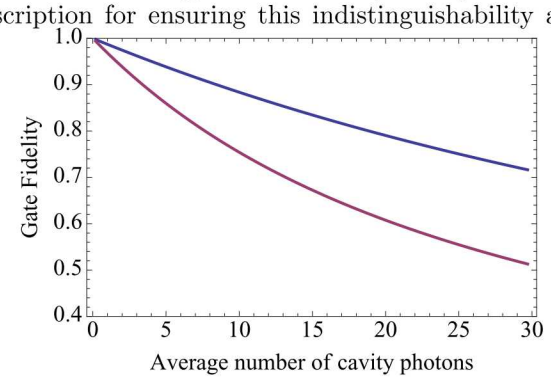

FIG. 8: (colour online) Gate fidelity for a $\pi/2$ σ_x pulse as a function of the number of photons in a given cavity. The measurement dephasing rate k is calculated from the photon number using $k = \frac{4|\alpha|^2\chi^2}{\kappa^3}$. The blue line corresponds to a 10ns pulse while the red is for 40ns.

These results not only provide a theoretical framework for the remote probabilistic entanglement achieved experimentally in [18] but motivate other schemes. Of particular importance is continuous wave measurement, which is needed for longer and more complicated applications such as error correction protocols and feedback control. We have shown that in the weak coupling limit the main effect of simultaneous measurement and coherent control is a rotation of the axes of rotation and a weak decay channel. These are balanced by the need to rotate the qubits quickly in order to avoid pinning of the computational states due to measurement. Generalizations of this scheme to create multi-qubit entangled states and to generate entanglement deterministically using feedback will be addressed in future work.

[1] H. J. Kimble, Nature **453**, 1023 (2008).
[2] D. Gottesman and I. L. Chuang, Nature **402**, 390 (1999).
[3] M. Aspelmeyer, H. R. Böhm, T. Gyatso, T. Jennewein, R. Kaltenbaek, M. Lindenthal, G. Molina-Terriza, A. Poppe, K. Resch, M. Taraba, et al., Science **301**, 621 (2003).
[4] C.-Z. Peng, T. Yang, X.-H. Bao, J. Zhang, X.-M. Jin, F.-Y. Feng, B. Yang, J. Yang, J. Yin, Q. Zhang, et al.,

Physical Review Letters **94**, 150501 (2005).

[5] M. Lettner, M. Mücke, S. Riedl, C. Vo, C. Hahn, S. Baur, J. Bochmann, S. Ritter, S. Dürr, and G. Rempe, Phys. Rev. Lett. **106**, 210503 (2011), URL http://link.aps.org/doi/10.1103/PhysRevLett.106.210503.

[6] S. Ritter, C. Nölleke, C. Hahn, A. Reiserer, A. Neuzner, M. Uphoff, M. Mucke, E. Figueroa, J. Bochmann, and G. Rempe, Nature **484**, 195 (2012).

[7] C. Cabrillo, J. I. Cirac, P. García-Fernández, and P. Zoller, Phys. Rev. A **59**, 1025 (1999), URL http://link.aps.org/doi/10.1103/PhysRevA.59.1025.

[8] S. Bose, P. L. Knight, M. B. Plenio, and V. Vedral, Phys. Rev. Lett. **83**, 5158 (1999), URL http://link.aps.org/doi/10.1103/PhysRevLett.83.5158.

[9] L.-M. Duan, M. D. Lukin, J. I. Cirac, and P. Zoller, Nature **414**, 413 (2001).

[10] X.-L. Feng, Z.-M. Zhang, X.-D. Li, S.-Q. Gong, and Z.-Z. Xu, Phys. Rev. Lett. **90**, 217902 (2003), URL http://link.aps.org/doi/10.1103/PhysRevLett.90.217902.

[11] C. Simon and W. T. M. Irvine, Phys. Rev. Lett. **91**, 110405 (2003), URL http://link.aps.org/doi/10.1103/PhysRevLett.91.110405.

[12] D. E. Browne, M. B. Plenio, and S. F. Huelga, Phys. Rev. Lett. **91**, 067901 (2003), URL http://link.aps.org/doi/10.1103/PhysRevLett.91.067901.

[13] C. W. Chou, H. de Riedmatten, D. Felinto, S. V. Polyakov, S. J. van Enk, and H. J. Kimble, Nature **438**, 828 (2005).

[14] D. L. Moehring, P. Maunz, S. Olmschenk, K. C. Younge, D. N. Matsukevich, L.-M. Duan, and C. Monroe, Nature **449**, 68 (2007).

[15] L.-M. Duan, J. I. Cirac, P. Zoller, and E. S. Polzik, Phys. Rev. Lett. **85**, 5643 (2000), URL http://link.aps.org/doi/10.1103/PhysRevLett.85.5643.

[16] S. Clark, A. Peng, M. Gu, and S. Parkins, Phys. Rev. Lett. **91**, 177901 (2003).

[17] B. Julsgaard, A. Kozhekin, and E. Polzik, Nature **413**, 400 (2001).

[18] N. Roch, M. E. Schwartz, F. Motzoi, C. Macklin, R. Vijay, A. W. Eddins, A. N. Korotkov, K. B. Whaley, M. Sarovar, and I. Siddiqi, Phys. Rev. Lett. **112**, 170501 (2014).

[19] C. W. Gardiner, Phys. Rev. Lett. **70**, 2269 (1993).

[20] H. J. Carmichael, Phys. Rev. Lett. **70**, 2273 (1993).

[21] J. E. Gough, Philosophical Transactions of the Royal Society A: Mathematical, Physical and Engineering Sciences **370**, 5241 (2012).

[22] J. Gambetta, J. Gambetta, A. Blais, A. Blais, M. Boissonneault, M. Boissonneault, A. A. Houck, A. A. Houck, D. I. Schuster, D. I. Schuster, et al., Phys. Rev. A **77**, 012112 (2008).

[23] J. Gough and M. R. James, Comm. Math. Phys. **287**, 1109 (2009).

[24] J. Gough and M. R. James, IEEE Trans. Aut. Control **54**, 2530 (2009).

[25] H. M. Wiseman and G. J. Milburn, *Quantum measurement and control* (Cambridge University Press, 2009).

[26] C. W. Gardiner and P. Zoller, *Quantum noise* (2004).

[27] S. Hill and W. K. Wootters, Phys. Rev. Lett. **78**, 5022 (1997).

[28] B. Misra and E. C. G. Sudarshan, J. Math. Phys. **18**, 756 (1977).